Study on the Effect of Secondary Air Layout on CO Reduction Performance in a 75 t/h Biomass CFB Boiler Burning Wheat Straw

Jun Zhang [1], Yanmin Li [1], Lin Mei [2,3], Xiaoliang Yu [1], Xun Lv [4], Jinping Wang [1,5], Jin Yan [1,6,*] and Rongyue Sun [1,5,*]

1 College of Energy and Power Engineering, Nanjing Institute of Technology, Nanjing 211167, China
2 Key Laboratory of Electromechanical Equipment Security in Western Complex Environment for State Market Regulation, Chongqing 401121, China
3 Chongqing Special Equipment Inspection and Research Institute, Chongqing 401121, China
4 Xizi Clean Energy Equipment Manufacturing Co., Ltd., Hangzhou 310021, China
5 Key Laboratory of Energy Thermal Conversion and Control of Ministry of Education, Southeast University, Nanjing 210096, China
6 Key Laboratory of Low-Grade Energy Utilization Technologies and Systems, Ministry of Education of PRC, Chongqing University, Chongqing 400044, China
* Correspondence: jinyan@njit.edu.cn (J.Y.); sunrongyue@njit.edu.cn (R.S.); Tel.: +86-18151004185 (J.Y.)

Abstract: Biomass fuels play an important role in the field of fluidized bed combustion, but due to the diversity and uncertainty of fuels, there are usually some problems of high CO emission that cannot be directly solved by combustion adjustment. In this paper, a 75 t/h biomass fluidized bed was taken as the research object. It was observed from the field test that the gas incomplete combustion loss reached 12.13% when mono-combustion of wheat straw was conducted, and the CO concentration in the exhaust gas exceeded 30k ppm. Combined with the CPFD numerical simulation, the combustion characteristics and influence of secondary air layout on CO reduction performance were discussed in detail. The results revealed that the gas temperature gradually increased along furnace height under the initial condition, and the maximum temperature was more than 1000 °C at furnace outlet. The air curtain of the secondary air jets was insufficient, and the wheat straw rose rapidly as it entered into the furnace. By arranging adjacent secondary air ports above each fuel-feeding inlet, the residence time of particles in the furnace could be significantly increased, thus, the furnace temperature distribution was more reasonable and the CO emission was reduced by 58.6%.

Keywords: fluidized bed; secondary air; wheat straw; CO emission

1. Introduction

Biofuels usually include agricultural and forestry wastes, such as straw, rice husk, peanut husk, and household garbage, accounting for about 15% of the global energy consumption. Compared with traditional fossil energy, biomass fuel has a short production cycle, high volatile content, and low pollutant emission [1], which can even achieve zero CO_2 emission [2]. Countries around the world have actively carried out applied technology research and realized the scale of industrial application. Among them, the circulating fluidized bed (CFB) boiler has the advantages of wide combustion adaptability, high combustion efficiency, good pollutant control, and flexible load regulation [3–5], which can well adapt to biomass fuel. Therefore, the CFB combustion technology is widely used in the field of biomass power generation.

Due to the complexity and diversity of biomass fuel, scholars have conducted much research on its gasification and pyrolysis characteristics. Calvo et al. [6] adopted rice straw to comprehensively study the changes of material quantity balance, energy balance, tar concentration, product gas composition, gas phase ammonia, chloride and potassium

concentration, bed material sintering, and gasification efficiency in the close-coupled boiler–gasifier systems. Gómez-Barea et al. [7] designed a three-stage fluidized bed gasifier with 81% gasification efficiency, 98% coke conversion rate, and 0.01 g/m^3 tar in the produced gas. Song et al. [8] used pine wood to carry out gasification and hydrogen production experiments in an interconnected fluidized bed gasifier, and the hydrogen production, biomass carbon gasification, biomass carbon combustion, and biomass carbon utilization were investigated, respectively. In addition, some scholars have studied the co-gasification characteristics of biomass and coal. Li et al. [9] focused on the co-gasification device, and carried out the whole process simulation from co-gasification to methanol and co-generation to reveal the impact of biomass and key operating parameters on process operation. Raj et al. [10] generated production gas through co-gasification of low-grade coal and long-leaf Mahua biomass, and the operating variables of the gasifier were optimized using the response surface method (RSM). Based on the fluidized bed system, some other studies [11,12] also discussed the characteristics of biomass fast pyrolysis and its advantages in carbon capture.

Combustion is another approach to treat biomass fuel; reasonable material feeding and operating parameters can ensure the full burning of biomass fuel. In the fluidized bed boiler, relevant research usually focuses on combustion optimization and adjustment. Żukowski et al. [13] investigated the detailed emission characteristics of gas pollutants from polymers and biomass in the bubbling fluidized bed reactor, and found that the increase in combustion temperature aggravated the oxidation of fuel-combined nitrogen and the conversion of NO to N_2 on the coke surface. Liu et al. [14] co-burned coal and biomass in the pressurized oxy–fuel fluidized bed to capture CO_2 in a low-cost and environmentally friendly way. The effects of key operating parameters, such as combustion pressure, temperature, and biomass mixture ratio, on the emissions of gaseous/solid pollutants and the conversion and distribution of nitrogen and sulfur were also analyzed. Karlström et al. [15] found that the air-staging had significant effect on NO_x reduction characteristics during biomass combustion in the industrial bubbling fluidized bed. After the secondary air jets, the conversion rate of fixed nitrogen (NO+HCN+NH_3) to N_2 reached 65%. In particular, some scholars have discussed the combustion characteristics [16,17], pollutant emission characteristics [18–20], operation optimization [21,22], and ash deposition [23–25] of wheat straw commonly used in fluidized bed boilers under mono-combustion or co-combustion conditions.

It is not difficult to find that less attention has been paid to CO emission in the process of direct combustion of biomass in a CFB boiler. Only in China, biomass CFB boilers often have problems, such as coking of the heating surface and severe wear of the water wall. Many biomass CFB boilers have adopted de-NO_x combustion technology, which could cause serious CO emissions problems when dealing with low-density fuels. These failures often lead to insufficient combustion in the boiler, uneven temperature of the heating surface, and insufficient penetration of the secondary air jet, resulting in low combustion efficiency and high CO emission, which is difficult to rectify through conventional combustion adjustment. This is also one of the main problems in biomass CFB boilers at present.

Therefore, a typical 75 t/h (rated evaporation capacity) biomass CFB boiler was investigated in this paper. Focusing on low-density biomass fuels, the CO emission problem was analyzed during mono-combustion of wheat straw through field test. Then, the gas–solid flow and combustion characteristics were explored using CPFD approach to investigate the incentives for high CO emission. The influence of secondary air layout on CO emissions was also discussed in detail, and an optimized secondary air arrangement was proposed. The results could improve the flexibility of biomass fuel and the absorption capacity of agricultural and forestry wastes, and provide an important reference for the air distribution optimization of various biomass CFB boilers.

2. Problem Description

2.1. Introduction to the Biomass CFB Boiler

The boiler is of high temperature and high pressure, natural circulation, and π-type arrangement of the whole steel frame. The primary air enters the boiler in three ways, namely, the air chamber, the feed pipe, and the loose air pipe. The secondary air outlets are designed to be on the upper two floors of the dense phase zone, with four outlets on the front wall and five outlets on the rear wall. The main design parameters of the boiler are shown in Table 1.

Table 1. Typical operating parameters of the biomass CFB boiler.

Items	Units	Values
BMCR	t/h	75
Superheater outlet pressure	MPa	9.8
Superheater outlet temperature	°C	540
Feed water temperature	°C	215
Boiler efficiency	%	89.9
Exhaust gas temperature	°C	132

2.2. Field Test

The design fuel of the boiler is wheat:corn:poplar branch = 0.6:0.1:0.3. Considering the local actual crop conditions and operation deficiencies, the working condition of burning wheat straw was adopted and tested, while in other operating conditions, such as mono-combustion of wood and corn, the gas temperature distribution was reasonable and both CO and NO_x emission were acceptable. The size of straw after crushing is 2–3 cm, and the maximum size is less than 15 cm. The ultimate analysis of the feeding fuel was conducted in a drying oven in the laboratory using the loss on the ignition method based on standard GB/T 31391-2015, and the proximate analysis of the feeding fuel was conducted based on standard GB/T 30732-2014. The test results of the feeding fuel and combustion efficiency are shown in Table 2.

Table 2. Test results of the feeding fuel and boiler combustion efficiency.

Items	Units	Design	Test
Boiler evaporation	t/h	75	78.8
C	wt.%, ar	25.85	22.79
H	wt.%, ar	3.47	3.17
O	wt.%, ar	24.09	22.60
N	wt.%, ar	0.46	0.58
S	wt.%, ar	0.13	0.11
Moisture	wt.%, ar	38.00	33.26
Ash	wt.%, ar	8.00	17.49
Volatile	wt.%, ar	44.40	33.06
Low heating value	kJ/kg	8761	7704
Solid incomplete combustion loss	%	1.16	3.30
Gas incomplete combustion loss	%	0.2	12.13
Heat radiation loss	%	0.80	0.76
Exhaust heat loss	%	7.34	9.00
Boiler efficiency	%	90.31	74.52

The experimental results showed that the combustion efficiency of the biomass fluidized bed unit was significantly lower than the design value, which was due to the CO emission at the exhaust range 12,500–45,000 ppm, with the average value of over 30,000 ppm, and the gas incomplete combustion loss q_3 reached 12.13%. Under the condition of sufficient air supply, the O_2 content at the exhaust ranged 4–6%, so the extremely high CO emission may be caused by the short residence time of fuel and uneven air–fuel mixing in the furnace. According to the test results of the aerodynamic field, the distributions of

primary air and secondary air were uniform, so it could be considered that there was a mismatch between the positions of secondary air jets and the gas–solid upflow. In addition, the test also revealed that the operating bed temperature was only about 660 °C, which was 100 °C lower than the design value. This was also because the density of the wheat straw was much lower than wood, board, or other biomass fuels, which were entrained by the fluidization air immediately after entering the furnace, so that the combustible could not be fully burned in the dense phase zone.

Because of this, the flue gas temperature at the upper part of the furnace reached 800 °C during the test, which was 100 °C higher than the design value. This strange gas temperature distribution resulted in the coking of the high-temperature superheater and blocking of the low-temperature superheater. According to the feedback from the power plant, high CO emissions only occurred when burning wheat straw, and flue gas emissions under other operating conditions, such as mono-combustion of corn, board, or other high-density fuels, were normal. Therefore, the above problems could be solved if a better air curtain could be formed at the cross-section through the optimization of the secondary air layout, so as to promote the blocking of upstream fuel, and to increase the residence time of fuel particles and, eventually, to reduce CO emissions. In addition, as chlorine in the feeding fuel affects the agglomeration and sintering of ash deposit, an optimal secondary air layout could promote more reasonable gas temperature distribution, thus, reducing the ash sintering situation as well.

3. Numerical Simulations

3.1. Model Setup

The numerical simulation was conducted by using Barracuda 17.4 based on the CPFD approach. Since only the furnace part needed to be calculated, the external circulating loop was not considered in this model. The BC connectors were used to connect the furnace outlets and the returning ports, and each secondary air port was introduced through the injection function. The corresponding model and grid generation are exhibited in Figure 1. The orange lines represent the actual geometric boundaries of the biomass CFB boiler, the blue lines represent the grid lines, and the black lines were manually adjusted to obtain better geometric shapes. In addition, the local regions, such as secondary air ports, furnace outlets, feeding ports and returning ports, were densified.
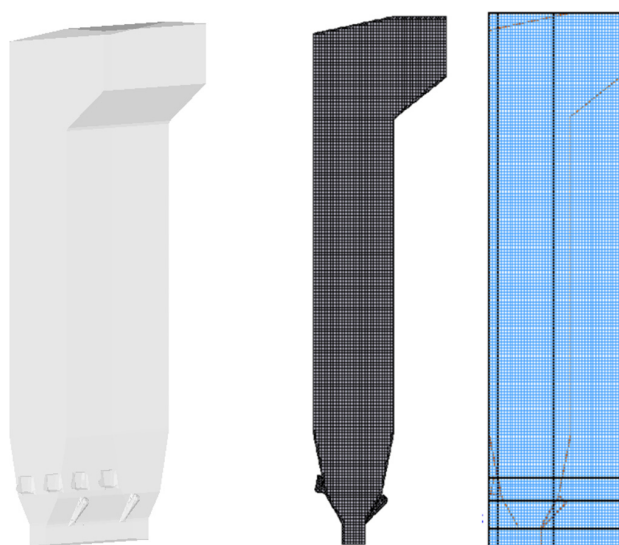
Figure 1. Model setup and grid generation of the biomass CFBB.

The mesh quality is exhibited in Figure 2. The mesh-generation method used in this paper regarded the entire boiler as a whole; each component was no longer divided separately but more attention has been paid to the unity of the grid. Considering the

times, cost, and accuracy requirements, grid encryption and independence verification were conducted on the basis of ensuring grid uniformity, as shown in Figure 3. When the mesh number increased from 457,968 to 550,120, there was no significant difference in solid concentration along the furnace height. Thus, the former 457,968 was finally selected.
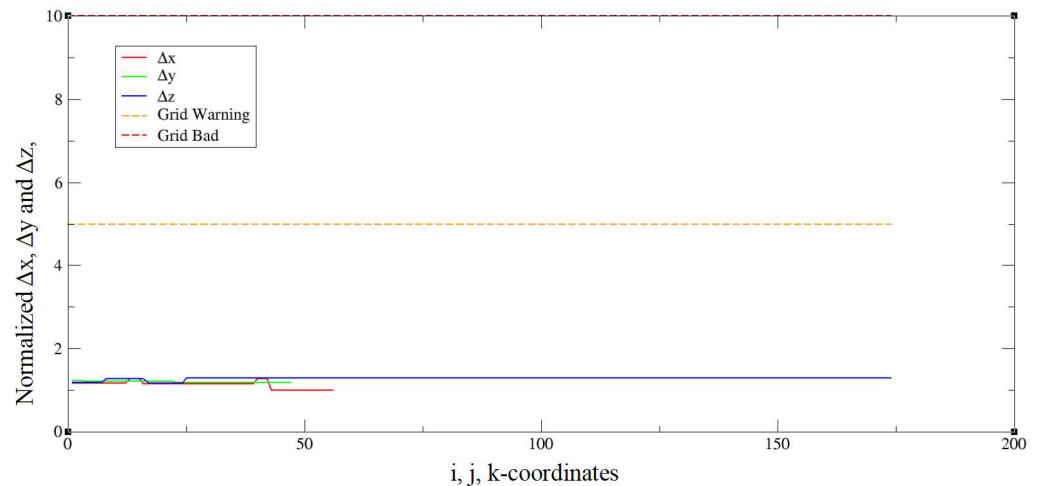
Figure 2. Mesh quality checking of this CFBB.
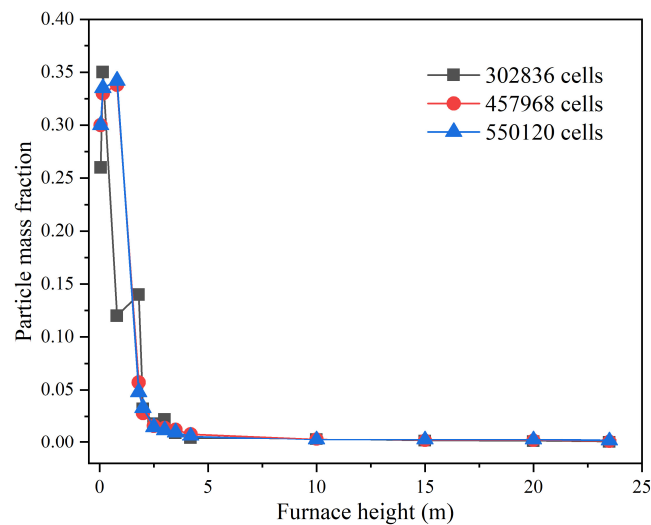
Figure 3. Mesh independence verification of this CFBB.

3.2. Numerical Simulation Method

The CPFD method was based on the MP-PIC (multiphase particle-in-cell) numerical calculation method. The Euler–Lagrange method was used to solve the three-dimensional motion of particles and fluids [26]. In this physical model, the fluid phase was treated by the Eulerian method, and the particle phase was treated by the MP-PIC numerical method. The motion equation of the solid phase was obtained by solving the transport equation of the particle distribution function in the MP-PIC method.

In the calculation process, the Wen–Yu–Ergun drag model was adopted to facilitate the calculation of drag force in the system with a large concentration gradient. The heterogeneous reaction involved in this paper included the combustion reaction of coke and the precipitation reaction of volatile matter. UDF was used to set the reaction rates of the above heterogeneous reactions and the relevant parameters of the external circulating ash were returned to the corresponding returning ports. The lumped heat equation was used to describe the energy equation of furnace particles, and the heat-transfer model adopted the particle-cluster renewal model, in which the radiation heat transfer only considered the

heat transfer between particles and the wall surface, without considering the heat transfer between particles. It should be noted that the field test indicated that the NO_x emission was no more than 10 mg/m^3, and this paper focused on CO generation and reduction performance. Therefore, more attention has been paid to the combustion of coke and volatile chemical reactions [27], without considering the generation of pollutants such as NO_x. Detailed governing equations and the heat-transfer model used in the numerical simulations are exhibited in Table 3.

Table 3. Governing equations and heat-transfer model in the numerical simulations.

Gas-phase continuous equation

$$\frac{\partial \theta_g \rho_g}{\partial t} + \nabla \left(\theta_g \rho_g u_g \right) = 0 \tag{1}$$

Gas-phase momentum equation

$$\frac{\partial \theta_g \rho_g}{\partial t} + \nabla \left(\theta_g \rho_g u_g \right) = -\frac{1}{\rho_g} \nabla P - \frac{1}{\rho_g} F + \theta_g g + \frac{1}{\rho_g} \nabla \tau \tag{2}$$

Gas-phase macroscopic stress tensor

$$F = \iiint f V_p \rho_p \left[D \left(u_g - u_p \right) - \frac{1}{\rho_p} \nabla P \right] dV_p d\rho du_p \tag{3}$$

Particle-phase momentum equation

$$\frac{du_p}{dt} = D \left(u_g - u_p \right) - \frac{1}{\rho_p} \nabla P + g - \frac{1}{\theta_p \rho_g} \nabla \tau_p \tag{4}$$

Particle normal stress model

$$\tau = \frac{P_s \theta_p^\beta}{\max \left[\left(\theta_{cp} - \theta_p \right), \varepsilon \left(1 - \theta_p \right) \right]} \tag{5}$$

Wen–Yu–Ergun drag model

$$\begin{aligned} D_1 &= 0.75 \theta_{cp} C_d > \theta_p \\ D_2 &= 0.85 \theta_{cp} C_d < \theta_p \\ 0.75 \theta_{cp} &\le \theta_p \le 0.85 \theta_{cp} C_d = \frac{\theta_p - 0.85 \theta_{cp}}{0.85 \theta_{cp} - 0.75 \theta_{cp}} (D_2 - D_1) + D_1 \end{aligned} \tag{6}$$

Radiative heat transfer between particles/fluid and the wall

$$q_{wp} = A_w F_{wp} \varepsilon_{wp} \sigma \left(T_w^4 - T_p^4 \right) \tag{7}$$

Convective heat transfer between the wall and fluid

$$\begin{aligned} h_{fw} &= h_1 + f_d h_d \\ h_d &= 1 - e^{-10(\theta_p / \theta_{cp})} \end{aligned} \tag{8}$$

Convective heat transfer between particles and fluid

$$h_p = \left[\left(c_0 \mathrm{Re}_L^{n_1} \mathrm{Pr}^{0.33} + c_1 \right) \frac{k_f}{d_p} + c_2 \right] \tag{9}$$

3.3. Boundary Condition Arrangements

The fuel properties were the same as the field test conditions. In this paper, two calculation conditions were considered—the original condition Case 1 and the optimization condition Case 2 based on the secondary air layout. In order to ensure the blocking effect of the secondary air on the fuel entering the furnace in the optimization condition, based on the test results and the preliminary analysis conclusions, the number of secondary air ports on the front wall of the first floor was increased from four to eight, and every two secondary air ports were arranged adjacent to each other and corresponded to one fuel-feeding port. Therefore, there were 22 secondary air ports after optimization. The key operating parameters and boundary conditions in thermal state are shown in Table 4.

Table 4. Key operating parameters of the numerical simulations.

Items	Units	Case 1	Case 2
Primary air	Nm^3/h	45,000	45,000
Secondary air	Nm^3/h	23,815	23,815
Level 1-SA-FW [1]	kg/s	2.69 (4 ports)	3.785 (8 ports)
Level 2-SA-FW	kg/s	2.69 (5 ports)	2.33 (5 ports)
Level 1-SA-RW [2]	kg/s	2.69 (5 ports)	2.33 (5 ports)
Level 2-SA-RW	kg/s	2.69 (4 ports)	2.33 (4 ports)
Fuel-feeding rate	kg/h	28,450	28,450

[1] SA—secondary air; FW—front wall; [2] RW—rear wall.

4. Results and Discussion

4.1. Distributions of Axial Particle Velocity in Case 1

Figure 4 exhibits the contours of particles axial velocity at different vertical sections in Case 1. Due to the low fuel density, the fuel entering the furnace would rapidly move upward at the inlets, and most particles in the furnace were in the upward state. Because of the secondary air injections, the fuel particles entering the furnace gradually rose from a certain depth from the front wall, and gradually moved to the front wall. In the area of the returning port, the circulating ash entering the furnace presented an obvious downward state close to the rear wall. It is also not difficult to see that the particles near the wall of each vertical section in the furnace presented a downward state, but the upward particles dominated. In addition, in the furnace outlet areas, obvious particle acceleration occurred at all key sections.
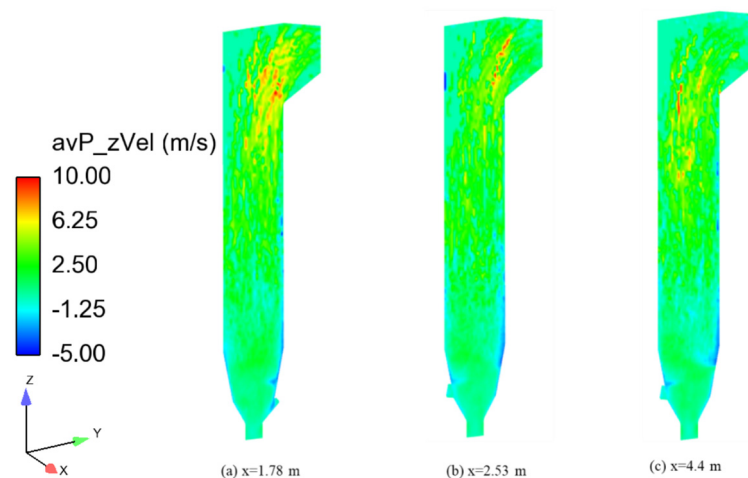
Figure 4. Contours of particles axial velocity at different vertical sections in Case 1 ((**a**)−returning port; (**b**)−secondary air port; (**c**)−fuel-feeding port).

4.2. Combustion Characteristics in Case 1

4.2.1. Gas Temperature Distributions in Case 1

Figure 5 shows the distributions of average flue gas temperature along the furnace height; the measured values of thermocouple temperature measurement ports at different heights are also displayed. Correction for radiation exchange with the surrounding cold wall was not necessary because the hot particle suspension around the probe protected it from radiation cooling. It can be seen that the two values were close and all exhibited a gradually increasing distribution, indicating the accuracy of the numerical results. Besides, as the particles and gas have different heat capacity, Figure 6 exhibits the temperature differences between the two phases. It can be seen that most particles gathered in the middle and lower parts of the furnace, but local high-temperature solid particles appeared in the dilute phase zone. It is believed that the biomass fuels had a high proportion of volatile combustion, so there were reasonable temperature differences between the particle and gas phase distributions.

Figure 7 shows the contours of flue gas temperature at key vertical sections. The bed temperature of this biomass CFB boiler was about 660 °C, which was significantly different from that of a conventional coal-fired fluidized bed. The gas temperature remained basically unchanged in the dense phase zone. With the increase in the furnace height, the average flue gas temperature gradually increased and reached over 1000 °C at the furnace outlet. The main reason was that the density of the fuel entering the furnace was lower than burning corn, board, or other high-density fuels, so the residence time in the furnace was short. Also, the gas temperature in the dense phase zone had no obvious sudden changes, indicating that the combustion share in the lower part of the furnace was low.
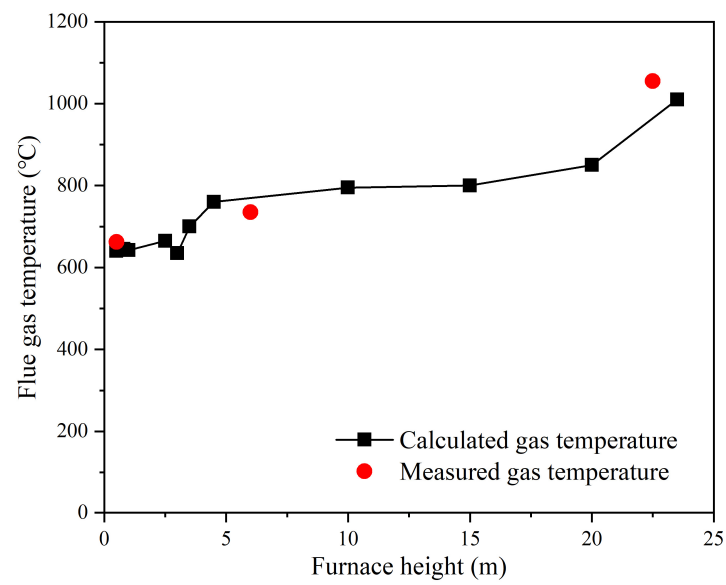
Figure 5. The average temperature of flue gas distributed along the furnace height in Case 1.
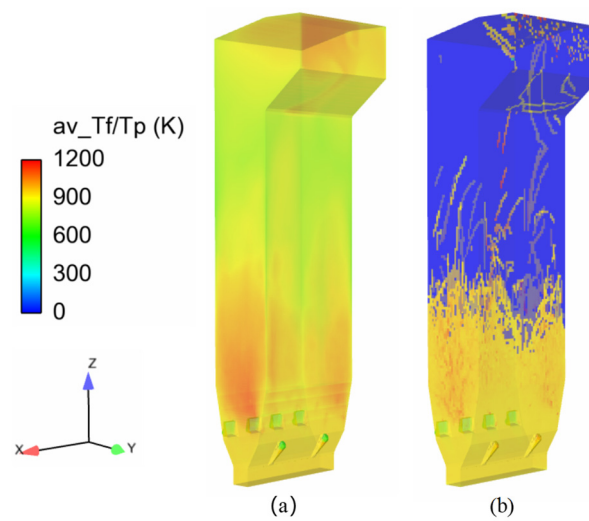
Figure 6. Temperature differences between the particles and gas phase ((**a**)—gas phase; (**b**)—particles).
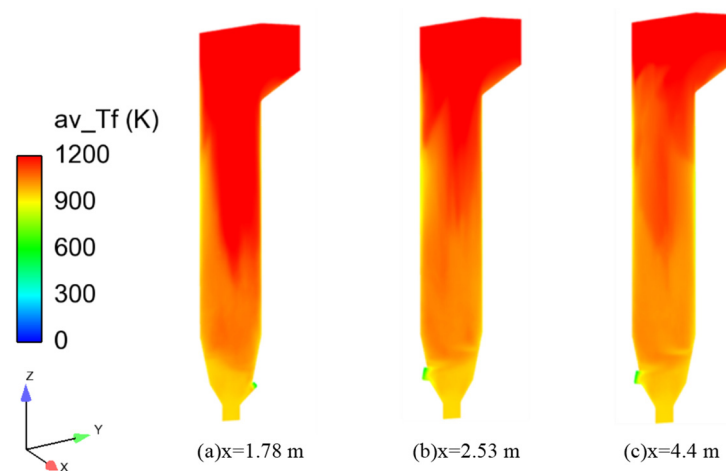
Figure 7. Contours of gas temperature distributions at key vertical sections in Case 1 ((**a**)−returning port; (**b**)−secondary air port; (**c**)−fuel-feeding port).

As can be observed from the contours of oxygen concentrations at key vertical sections in Figure 8, the blocking effect of secondary air was not good, resulting in the wheat straw being blown to the upper part of the furnace immediately from the area not covered by the secondary air section after entering the furnace, so that the flue gas temperature at the furnace outlet area continued to rise to the maximum value. The gas–solid mixing could be strengthened at the corner of the furnace outlet, so the flue gas temperatures were significantly increased. Under the initial condition (Case 1), the unreasonable distribution of combustion share would also aggravate the risk of coking on the upper heating surface of the furnace.
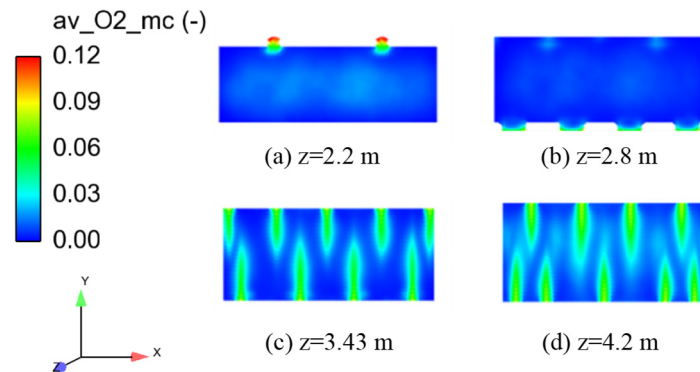
Figure 8. Distributions of oxygen concentration in cross-sections of dense phase zone in Case 1 ((**a**)—returning port; (**b**)—fuel-feeding port; (**c**)—lower secondary air; (**d**)—upper secondary air).

4.2.2. CO Distributions in Case 1

Figure 9 exhibits the three-dimensional contour of CO concentration in Case 1. It can be seen that the distribution of CO concentration along the furnace height generally presented a trend of gradual decrease. The CO concentrations in the dense phase zone were the highest with a value of over 70,000 mg/m^3. Due to the low fuel density and short residence time in the furnace, the burnout rate of the feeding fuel was low, resulting in high CO concentration in the whole furnace. Even in the furnace outlet areas, the CO concentration still reached 22,650 mg/m^3.
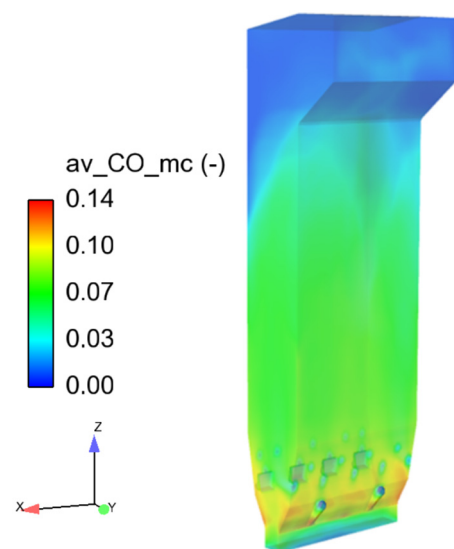
Figure 9. Three-dimensional contour of CO concentration in Case 1.

According to the recorded measurement results, the average CO concentration at the exhaust exceeded 30,000 ppm. It is analyzed that the feeding ports were extremely prone to clogging, resulting in abnormal fluctuations in the actual CO emissions, so the measured

results were higher than the calculated values. However, they were in the same order of magnitude, indicating the irrationality of CO emissions. Combined with the contours of CO concentration distributions in the key vertical sections, as shown in Figure 10, it was observed that the CO concentration near the height of the feeding inlet was relatively high. Since no fuel air was set near the fuel-feeding port, the gas–solid mixing is not strong enough, resulting in high CO concentration. This high value continued to the upper part of the furnace until the CO concentration at the furnace outlet decreased, indicating that the absorption capacity of CO at the dilute phase zone of the furnace was weak. Therefore, it was necessary to consider reducing the CO generations in the dense phase zone during the optimization. The gas–solid mixing should be strengthened by promoting the disturbance in the dense phase zone, so as to obtain better CO reduction performance.
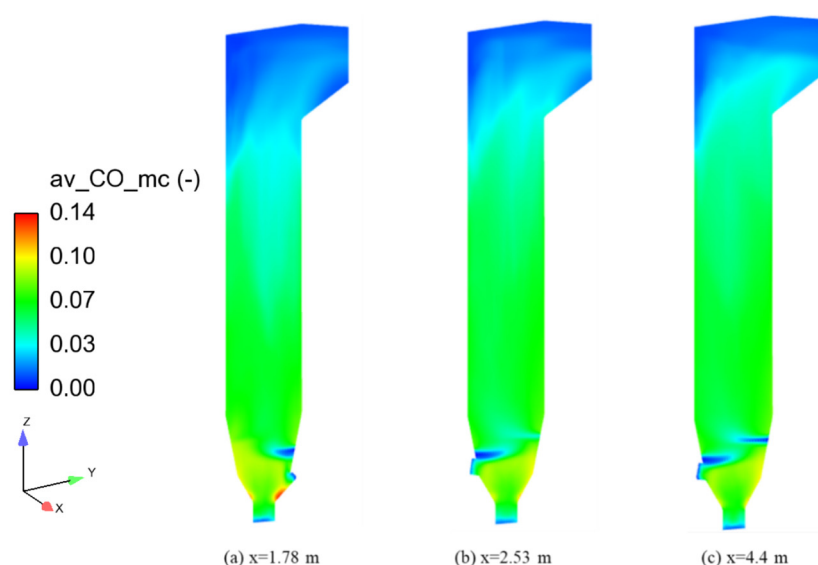
Figure 10. Contours of CO concentration at key vertical sections of the biomass CFB boiler in Case 1 ((**a**)−returning port; (**b**)−secondary air port; (**c**)−fuel-feeding port).

4.3. Combustion Characteristics in Case 2

4.3.1. Temperature Distributions in Case 2

Figure 11 represents the gas temperature profile along furnace height in Case 2. It can be seen that although the flue gas temperature along the height direction of the furnace still presented a gradually rising distribution trend, the bed temperature increased by 20–30 °C, and the increase in flue gas temperature in the dilute phase zone was significantly weakened. At furnace outlet, the flue gas temperature was no more than 900 °C, thus, alleviating the coking of the upper heating surface of the furnace.

According to the distributions of oxygen concentration in the vertical sections, as shown in Figure 12, the area near the cross-section of the returning port was still in a serious reducing condition, this state also appeared at the cross-section of the lower secondary air ports. However, the coverage area of the secondary air was better than the initial condition, and the layout of the adjacent secondary air ports above the fuel-feeding port could effectively block the rapid upward movement of the feeding fuel. In addition, the reducing condition at the cross-section of the upper secondary air ports showed to be further relieved. The blocking effect of the lower secondary air on the front wall and the upper secondary air on the rear wall, as well as the upper secondary air on the front wall and the lower secondary air on the rear wall, could increase the residence time of the feeding fuel in the dense phase zone. This layout of secondary air ports had two effects; one was the blocking and combustion supporting effect of the gas–solid upward flow, and the other was the uniformity of the oxygen concentration distribution at the subsequent furnace outlet, which could cover the furnace depth and cause the oxygen distribution to be more uniform in the areas above the height of secondary air ports.
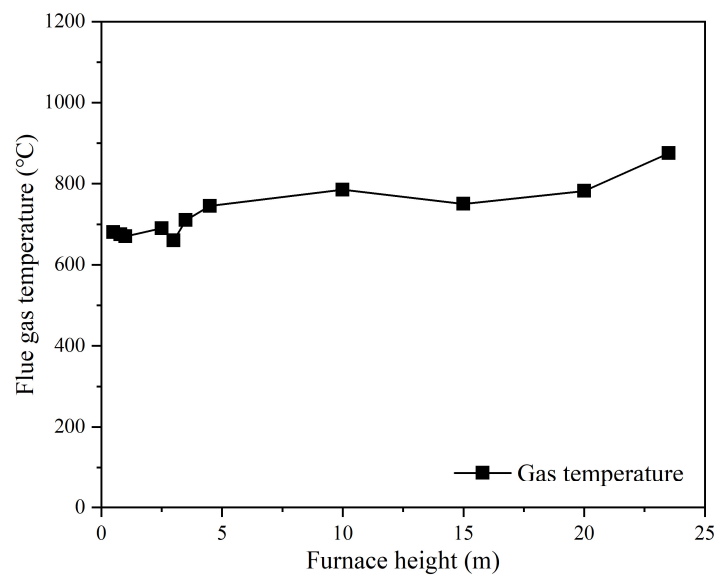
Figure 11. The average temperature of flue gas distributed along the furnace height in Case 2.
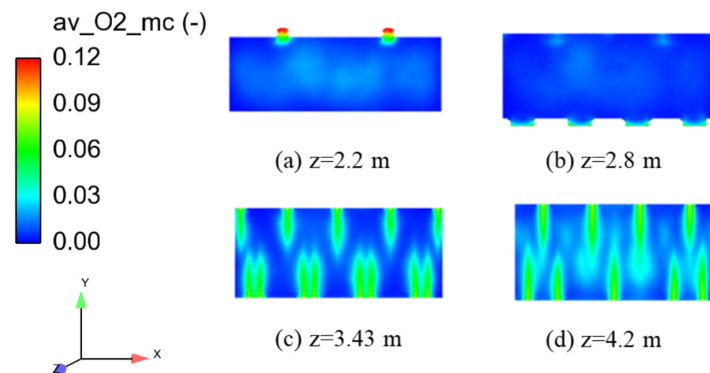
Figure 12. Distributions of oxygen concentration in cross-sections of dense phase zone in Case 2 ((**a**)—returning port; (**b**)—fuel-feeding port; (**c**)—lower secondary air; (**d**)—upper secondary air).

4.3.2. CO Emission in Case 2

Figure 13 exhibits the three-dimensional contour of CO concentration in Case 2. It could be seen that the CO concentration in the direction of furnace height generally presented a gradually decreasing trend, and the CO concentration in the dense phase zone was the highest, with a value of over 70,000 mg/m^3, which was consistent with the initial condition.

Compared with Figure 6, the most obvious area of CO emission reduction was the dilute phase zone of the furnace, which was mainly due to the improved secondary air layout, especially the secondary air ports above the front wall feed inlet which could enhance the gas–solid mixing and improve the residence time of materials in the dense phase zone. According to the calculation results of the average section value, the CO concentration at the furnace outlet section was 9375 mg/m^3, which was 58.6% lower than the initial condition. It could be proposed that under the condition of ensuring the same total secondary air volume, CO emissions could be significantly reduced by optimizing the secondary air layout. In addition, Table 5 presents the comparisons of CO reduction measures and performance with previous studies. It could be seen that the two biomass CFB boilers used wood with higher density as feeding fuel, while the initial CO emission still reached 7000 and 13,177, respectively. In order to reduce CO emission, measures such as reducing bed pressure and increasing SA flow rates, especially the nozzles on the front wall (fuel-feeding side), were mainly adopted. These ideas were similar to this boiler, but more serious CO emission was bound to occur when burning wheat straw with

lower density. Seen from CO emissions and distributions in Case 1 and Case 2, it could be concluded that ensuring the penetration depth of secondary air cannot form a dense air curtain, so the fuel particles would, inevitably, rise rapidly from the gaps between the air jets and escape from the furnace outlet, thereby reducing the residence time of particles. In other words, it was not enough if simply increasing the flow rate of SA on the front wall. Also, the decrease in CO concentration mainly occurred in the dilute phase zone, so increasing the residence time of fuel in the dense phase zone could also promote a fully mixing of combustibles and air, resulting in better burnout in the higher part of the CFB furnace. Judged from Case 2, it is revealed that the most effective layout of secondary air ports was to ensure the full mixing of particles in the fuel inlet area, and it is necessary to arrange more secondary air ports directly above the fuel-feeding port.
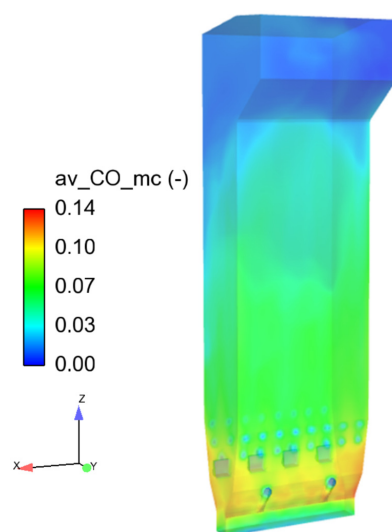
Figure 13. Three-dimensional contour of CO concentration in Case 2.

Table 5. Comparisons of CO reduction measures and performance with previous works.

Ref.	Fuel Type	BMCR (t/h)	Initial CO (mg/m^3)	Optimized CO (mg/m^3)	Measures
[28]	Wood	75	7000	2350	(1) Bed pressure ↓ (2) SA-FW ↑
[29]	Wood	220	13,177	5002	(1) Excess air coefficient ↑ (2) PA/SA ratio ↓ (3) Fuel drying
This work	Wheat straw	75	28,313	9375	SA layout optimization

4.4. Additional Consideration

According to the field test and numerical calculation results of combustion and CO emission in the furnace, further improvement of CO-reduction performance can be considered from the following aspects:

(1) If more levels of secondary air ports are set, the gas–solid mixing can be better promoted but the CO emissions are unpredictable. Although CO-emission reduction is reflected in the dilute phase zone, increasing the residence time and mixing of fuel in the dense phase zone is the key and foundation based on the above analysis. Also, the extra layout of secondary air ports will dilute the secondary air flow rate of a single port, resulting in a weaker blocking effect of air jets, accelerated fuel escape, and shorter residence time of particles;

(2) There is a high CO concentration area near the front wall due to the influence of secondary air. Reducing the height of the fuel-feeding ports can promote better

combustion, while the local CO concentration will also increase. If the appropriate air supply and primary air/secondary air ratio are selected through combustion adjustment, the combustion share and bed temperature in the dense phase zone can be increased while the CO concentration is still under control;

(3) In order to reduce CO emissions, the adjustment strategy is to increase the secondary air rate, especially the secondary air volume of the front wall. For biomass fuels with low density, simple combustion adjustments cannot meet the requirements, so it is necessary to consider additional secondary air layout to block the fuels and the cooperation with secondary air ports at higher levels;

(4) Under the condition that the secondary air volume remains unchanged, the additional part introduced from the primary air is arranged above each fuel-feeding port as the fuel air, which can not only increase the combustion share, but also reduce the fuel gasification in the dense phase zone, and, finally, reduce the local CO concentration.

5. Conclusions

In this paper, the CO-emission characteristics of a biomass CFB boiler burning wheat straw was investigated through field tests. The gas–solid flow, combustion characteristics, and the influence of the secondary air layout on CO emissions were then discussed in detail by using the CPFD approach, and the following conclusions were obtained.

(1) Due to the serious deviation of the actual fuel from the design mixing ratio, when the low-density fuel such as wheat straw was mono-combusted, the NO_x emission was acceptable but the CO concentration in the exhaust gas exceeded 30,000 ppm, and the gas incomplete combustion loss reached 12.13%. It was believed that there was a mismatch between the positions of the secondary air jets and the gas–solid upflow;

(2) The numerical results of the initial condition revealed that the gas temperature showed a gradual upward trend, and the value exceeded 1000 °C at the furnace outlet. The layout of secondary air was unreasonable and the dilute phase zone had insufficient CO absorption capacity. The calculated CO concentration at the furnace outlet still reached 22,650 mg/m^3;

(3) With the total secondary air volume unchanged, the bed temperature increased by 20–30 °C and the flue gas temperature at the furnace outlet was less than 900 °C after the number of secondary air ports on the front wall increased from four to eight. The adjacent secondary air layout above the fuel-feeding port could effectively block the upward flow of the material. The CO concentration at the furnace outlet was decreased by 58.6% with a value of 9375 mg/m^3. The increase residence time of fuel particles in the dense phase zone could promote better gas—solid mixing and CO reduction performance in the upper furnace;

(4) The most effective layout of secondary air ports was to ensure the full mixing of particles in the fuel-inlet area, and it was necessary to arrange more secondary air ports directly above the fuel-feeding port. Future work could focus on the layout and joint operation of fuel-feeding air, as well as its impact on the dispersion and mixing of low-density biomass fuels in the dense phase zone.

Author Contributions: Conceptualization, J.Y. and J.Z.; investigation, J.Z., J.Y. and R.S.; methodology, J.Y. and Y.L.; writing—original draft preparation, J.Z.; writing—review and editing, J.Y., L.M., X.L. and X.Y.; validation, Y.L., J.W. and R.S.; software, J.Y. and Y.L. All authors have read and agreed to the published version of the manuscript.

Data Availability Statement: Not applicable.

Conflicts of Interest: The authors declare no conflict of interest.

Nomenclature

A_w	Wall area, m^2
D_p	Drag force, N
d_p	Particle size, m
F	Gas-phase macroscopic stress tensor, N
F_{wp}	Effective emissivity between the wall and the particles
h_1	Heat-transfer coefficient of the dilute phase zone
h_d	Heat-transfer coefficient of the dense phase zone
k_f	Thermal conductivity of the fluid
p	Gas-phase pressure, Pa
p_s	Material parameter
Re_p	Reynolds number of the particles
u_g	Gas-phase velocity, m/s
u_p	Particle velocity, m/s
Greek symbols	
ρ_p	Particle density, kg/m^3
ρ_g	Gas-phase density, kg/m^3
θ_g	Volume fraction of the gas phase
θ_{cp}	Volume fraction when the particles are closely packed
τ	Momentum exchange rate of the gas phase and the particle phase per unit volume
τ_p	Particle normal stress, N
ε_{wp}	Boltzmann's constant

References

1. Ke, X.; Zhang, Y.; Liu, X.; Wu, Y.; Huang, Z.; Zhang, M.; Lyu, J.; Zhou, T. Development of biomass-fired circulating fluidized bed boiler with high steam parameters based on theoretical analysis and industrial practices. *J. Energy Inst.* **2022**, *105*, 415–423. [CrossRef]
2. Szul, M.; Iluk, T.; Zuwała, J. Use of CO_2 in Pressurized, Fluidized Bed Gasification of Waste Biomasses. *Energies* **2022**, *15*, 1395. [CrossRef]
3. Miao, M.; Zhou, T.; Zhang, M.; Bai, R.; Yang, H. Transformation of CFB boilers pollutant treatment strategies under China's stricter requirements and the background of carbon neutrality. *Fuel* **2022**, *342*, 127009. [CrossRef]
4. Leckner, B. Negative CO_2 emission from oxy-fuel combustion in CFB boilers. *Fuel* **2023**, *333*, 126425. [CrossRef]
5. Xin, S.; Wang, H.; Li, J.; Wang, G.; Wang, Q.; Cao, P.; Zhang, P.; Lu, X. Discussion on the Feasibility of Deep Peak Regulation for Ultra-Supercritical Circulating Fluidized Bed Boiler. *Energies* **2022**, *15*, 7720. [CrossRef]
6. Calvo, L.; Gil, M.; Otero, M.; Morán, A.; García, A. Gasification of rice straw in a fluidized-bed gasifier for syngas application in close-coupled boiler-gasifier systems. *Bioresour. Technol.* **2012**, *109*, 206–214. [CrossRef]
7. Gómez-Barea, A.; Leckner, B.; Perales, A.V.; Nilsson, S.; Fuentes-Cano, D. Improving the performance of fluidized bed biomass/waste gasifiers for distributed electricity: A new three-stage gasification system. *Appl. Therm. Eng.* **2011**, *50*, 1453–1462. [CrossRef]
8. Song, T.; Wu, J.; Shen, L.; Xiao, J. Experimental investigation on hydrogen production from biomass gasification in interconnected fluidized beds. *Biomass Bioenergy* **2012**, *36*, 258–267. [CrossRef]
9. Li, S.; Sun, X.; Liu, L.; Du, J. A full process optimization of methanol production integrated with co-generation based on the co-gasification of biomass and coal. *Energy* **2023**, *267*, 126566. [CrossRef]
10. Raj, R.; Singh, D.K.; Tirkey, J. Co-gasification of Low-grade coal with Madhuca longifolia (Mahua) biomass and dual-fuelled mode engine performance: Effect of biomass blend and engine operating condition. *Energy Convers. Manag.* **2022**, *269*, 116150. [CrossRef]
11. Li, B.; Song, M.; Xie, X.; Wei, J.; Xu, D.; Ding, K.; Huang, Y.; Zhang, S.; Hu, X.; Zhang, S.; et al. Oxidative fast pyrolysis of biomass in a quartz tube fluidized bed reactor: Effect of oxygen equivalence ratio. *Energy* **2023**, *270*, 126987. [CrossRef]
12. Zhou, C.; Chen, L.; Liu, C.; Wang, J.; Xing, X.; Liu, Y.; Chen, Y.; Chao, L.; Dai, J.; Zhang, Y.; et al. Interconnected pyrolysis and gasification of typical biomass in a novel dual fluidized bed. *Energy Convers. Manag.* **2022**, *271*, 116323. [CrossRef]
13. Żukowski, W.; Jankowski, D.; Wrona, J.; Berkowicz-Płatek, G. Combustion behavior and pollutant emission characteristics of polymers and biomass in a bubbling fluidized bed reactor. *Energy* **2023**, *263*, 125953. [CrossRef]

14. Liu, Q.; Zhong, W.; Yu, A.; Wang, C.-H. Co-firing of coal and biomass under pressurized oxy-fuel combustion mode in a 10 kWth fluidized bed: Nitrogen and sulfur pollutants. *Chem. Eng. J.* **2022**, *450*, 138401. [CrossRef]

15. Karlström, O.; Vainio, E.; Engblom, M.; Brink, A.; Hupa, M. Effect of air staging on NO$_x$ emissions in biomass combustion in a bubbling fluidized bed. *Fuel* **2022**, *330*, 125565. [CrossRef]

16. Yang, Q.; Wang, T.; Wang, J.; Sui, Z.; Wang, L.; Zhang, Y.; Pan, W.-P. Combustion, emission and slagging characteristics for typical agricultural crop straw usage in heating plants. *Thermochim. Acta.* **2021**, *702*, 178979. [CrossRef]

17. Cheng, G.; Zhao, Y.; Pan, S.; Wang, X.; Dong, C. A comparative life cycle analysis of wheat straw utilization modes in China. *Energy* **2020**, *194*, 116914. [CrossRef]

18. Xue, Z.; Zhong, Z.; Lai, X. Investigation on gaseous pollutants emissions during co-combustion of coal and wheat straw in a fluidized bed combustor. *Chemosphere* **2019**, *240*, 124853. [CrossRef] [PubMed]

19. Ulusoy, B.; Anicic, B.; Lin, W.; Lu, B.; Wang, W.; Dam-Johansen, K.; Wu, H. Interactions in NOX chemistry during fluidized bed co-combustion of residual biomass and sewage sludge. *Fuel* **2021**, *294*, 120431. [CrossRef]

20. Sheikh, K.; Khan, M.; Hamid, M.; Shrestha, S.; Ali, B.; Ryabov, G.; Dolgushin, L.A.; Hussain, M.A.; Bukharkina, T.V. Advances in reduction of NO$_x$ and N$_2$O emission formation in an oxy-fired fluidized bed boiler. *Chinese J. Chem. Eng.* **2019**, *27*, 426–443. [CrossRef]

21. Yang, R.; Ma, C.; Chen, G.; Cheng, Z.; Yan, B.; Mansour, M. Study on NO$_x$ emission during corn straw/sewage sludge co-combustion: Experiments and modelling. *Fuel* **2021**, *285*, 119208. [CrossRef]

22. Milićević, A.; Belošević, S.; Crnomarković, N.; Tomanović, I.; Tucaković, D. Mathematical modelling and optimisation of lignite and wheat straw co-combustion in 350 MWe boiler furnace. *Appl. Energy* **2019**, *260*, 114206. [CrossRef]

23. Morris, J.D.; Daood, S.S.; Nimmo, W. The use of kaolin and dolomite bed additives as an agglomeration mitigation method for wheat straw and miscanthus biomass fuels in a pilot-scale fluidized bed combustor. *Renew. Energy* **2022**, *196*, 749–762. [CrossRef]

24. Morris, J.D.; Daood, S.S.; Nimmo, W. Agglomeration and the effect of process conditions on fluidized bed combustion of biomasses with olivine and silica sand as bed materials: Pilot-scale investigation. *Biomass Bioenergy* **2020**, *142*, 105806. [CrossRef]

25. Zhai, M.; Li, X.; Yang, D.; Ma, Z.; Dong, P. Ash fusion characteristics of biomass pellets during combustion. *J. Clean. Prod.* **2022**, *336*, 130361. [CrossRef]

26. Chang, J.; Ma, X.; Wang, X.; Li, X. Computational particle fluid dynamics modeling and design of in-situ catalytic deNO$_x$ in an industrial CFB boiler. *Chem. Eng. Sci.* **2023**, *270*, 118502. [CrossRef]

27. Yan, J.; Lu, X.; Xue, R.; Lu, J.; Zheng, Y.; Zhang, Y.; Liu, Z. Validation and application of CPFD model in simulating gas-solid flow and combustion of a supercritical CFB boiler with improved inlet boundary conditions. *Fuel Process. Technol.* **2020**, *208*, 106512. [CrossRef]

28. Sun, J.; Liu, X.; Dai, G.; Zhao, X.; Zheng, S.; Xue, D.; Rahman, Z.; Wang, X. Characterization of NO$_x$ and greenhouse gas emissions in a 15 MW biomass circulating fluidized bed. *Clean Coal Technol.* **2023**, 1–7.

29. Wang, P.; Li, D. Experimental study of combustion optimization and adjustment of 50 MW biomass circulating fluidized bed boiler. *Ind. Boiler* **2021**, *6*, 49–53.